ARTICLE

Massive water production from lunar ilmenite through reaction with endogenous hydrogen

Xiao Chen,[1,2,9] Shiyu Yang,[1,2,9] Guoxin Chen,[3,9] Wei Xu,[1,9] Lijian Song,[1] Ao Li,[1] Hangboce Yin,[1] Weixing Xia,[1] Meng Gao,[1] Ming Li,[3] Haichen Wu,[3] Junfeng Cui,[3] Lei Zhang,[3] Lijing Miao,[3] Xiaoxue Shui,[3] Weiping Xie,[3] Peiling Ke,[3] Yongjiang Huang,[4] Jianfei Sun,[4] Bingnan Yao,[1] Min Ji,[1] Mingliang Xiang,[1] Yan Zhang,[1,2] Shaofan Zhao,[5] Wei Yao,[5] Zhigang Zou,[5,6] Mengfei Yang,[5] Weihua Wang,[2,5,7,8] Juntao Huo,[1,2,*] Jun-Qiang Wang,[1,2,*] and Haiyang Bai[2,5,7,*]

*Correspondence: huojuntao@nimte.ac.cn (J.H.); jqwang@nimte.ac.cn (J.-Q.W.); hybai@iphy.ac.cn (H.B.)

Received: July 24, 2024; Accepted: August 17, 2024; Published Online: August 22, 2024; https://doi.org/10.1016/j.xinn.2024.100690

GRAPHICAL ABSTRACT

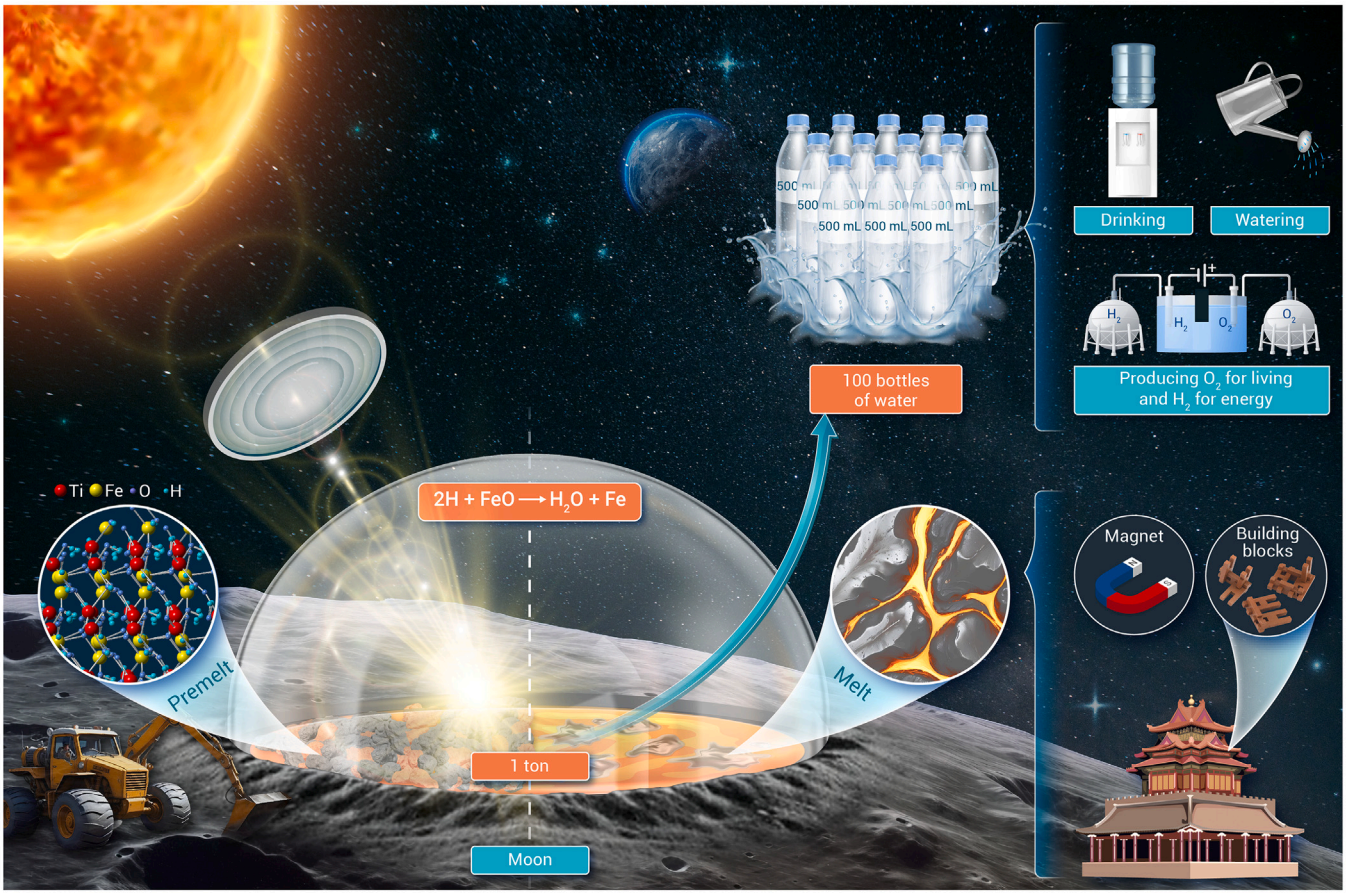

PUBLIC SUMMARY

- The hydrogen retained in lunar minerals is a substantial material for producing water on the Moon.
- More than 50 kg of water can be produced from 1 ton of lunar regolith after melting at temperatures above 1,200 K.
- Ilmenite contains the most hydrogen among the five primary lunar minerals.
- Concurrent formation of iron (Fe) crystals and H_2O bubbles is observed for the first time in *in situ* heating experiments.
- Electron irradiation can enhance the endogenous redox reaction between H and lunar regolith.

ARTICLE

Massive water production from lunar ilmenite through reaction with endogenous hydrogen

Xiao Chen,[1,2,9] Shiyu Yang,[1,2,9] Guoxin Chen,[3,9] Wei Xu,[1,9] Lijian Song,[1] Ao Li,[1] Hangboce Yin,[1] Weixing Xia,[1] Meng Gao,[1] Ming Li,[3] Haichen Wu,[3] Junfeng Cui,[3] Lei Zhang,[3] Lijing Miao,[3] Xiaoxue Shui,[3] Weiping Xie,[3] Peiling Ke,[3] Yongjiang Huang,[4] Jianfei Sun,[4] Bingnan Yao,[1] Min Ji,[1] Mingliang Xiang,[1] Yan Zhang,[1,2] Shaofan Zhao,[5] Wei Yao,[5] Zhigang Zou,[5,6] Mengfei Yang,[5] Weihua Wang,[2,5,7,8] Juntao Huo,[1,2,*] Jun-Qiang Wang,[1,2,*] and Haiyang Bai[2,5,7,*]

[1]Key Laboratory of Magnetic Materials and Devices, Ningbo Institute of Materials Technology and Engineering, Chinese Academy of Sciences, Ningbo 315201, China
[2]Center of Materials Science and Optoelectronics Engineering, University of Chinese Academy of Sciences, Beijing 100049, China
[3]Center of Test and Analysis, Ningbo Institute of Materials Technology and Engineering, Chinese Academy of Sciences, Ningbo 315201, China
[4]School of Materials Science and Engineering, Harbin Institute of Technology, Harbin 150001, China
[5]Qian Xuesen Laboratory of Space Technology, China Academy of Space Technology (CAST), Beijing 100049, China
[6]College of Engineering and Applied Science, Nanjing University, Nanjing 210093, China
[7]Institute of Physics, Chinese Academy of Sciences, Beijing 100049, China
[8]Songshan Lake Materials Laboratory, Dongguan 523830, China
[9]These authors contributed equally
*Correspondence: huojuntao@nimte.ac.cn (J.H.); jqwang@nimte.ac.cn (J.-Q.W.); hybai@iphy.ac.cn (H.B.)

Received: July 24, 2024; Accepted: August 17, 2024; Published Online: August 22, 2024; https://doi.org/10.1016/j.xinn.2024.100690

Citation: Chen X., Yang S., Chen G., et al., (2024). Massive water production from lunar ilmenite through reaction with endogenous hydrogen. The Innovation **5(5)**, 100690.

Finding water resources is a crucial objective of lunar missions. However, both hydroxyl (OH) and natural water (H_2O) have been reported to be scarce on the Moon. We propose a potential method for obtaining water on the Moon through H_2O formation via endogenous reactions in lunar regolith (LR), specifically through the reaction $FeO/Fe_2O_3 + H \rightarrow Fe + H_2O$. This process is demonstrated using LR samples brought back by the Chang'E-5 mission. FeO and Fe_2O_3 are lunar minerals containing Fe oxides. Hydrogen (H) retained in lunar minerals from the solar wind can be used to produce water. The results of this study reveal that 51–76 mg of H_2O can be generated from 1 g of LR after melting at temperatures above 1,200 K. This amount is ~10,000 times the naturally occurring OH and H_2O on the Moon. Among the five primary minerals in LR returned by the Chang'E-5 mission, $FeTiO_3$ ilmenite contains the highest amount of H, owing to its unique lattice structure with sub-nanometer tunnels. For the first time, *in situ* heating experiments using a transmission electron microscope reveal the concurrent formation of Fe crystals and H_2O bubbles. Electron irradiation promotes the endogenous redox reaction, which is helpful for understanding the distribution of OH on the Moon. Our findings suggest that the hydrogen retained in LR is a significant resource for obtaining H_2O on the Moon, which is helpful for establishing a scientific research station on the Moon.

INTRODUCTION

Water (H_2O) on the lunar surface is of significant interest owing to its crucial role in human survival. Infrared reflectance spectra from missions such as Cassini, Deep Impact, and Chandrayaan-1[1–4] have revealed the widespread presence of H_2O, predominantly as hydroxyl (OH). These near-infrared spectra have facilitated detailed analyses of the lunar water's latitude[3,5] and diurnal dependencies,[5,6] as well as the compositional characteristics of the water. Evaluations of lunar regolith (LR) samples have confirmed the presence of H_2O within agglutinitic glass,[7] volcanic glass,[8] and plagioclase.[9] However, these sources of H_2O are limited to concentrations ranging from 10 to 1,000 ppm, thus highlighting the need to identify more abundant lunar H_2O reservoirs.

The presence of solar-wind-implanted hydrogen (H) on the Moon has led to the hypothesis that redox reactions between H and oxide minerals might produce H_2O. The Chang'E-5 (CE-5) mission, in contrast to its predecessors, Apollo and Luna, targeted a high-latitude landing site in the northeastern Oceanus Procellarum basin (43.06°N, 51.92°W),[10] which is known for its elevated H concentration.[3,5,11] However, recent analyses[12–15] suggest that the CE-5 LR samples are exceptionally dry, with an H_2O content of only 283 ppm.[16] This low H_2O content observed in the CE-5 samples is attributable to their relatively younger age compared with samples from the Apollo and Luna missions.[17] Consequently, there has been less reaction between H and lunar oxides.[18,19] Additionally, the characteristics of LR particles affect the retention of H from solar proton implantation.[7,20–26] The regolith returned by the CE-5 mission presents a unique opportunity to further investigate lunar H and H_2O resources.[27,28] Studying the potential production of H_2O from redox reactions between implanted H and oxides, as well as identifying minerals with higher H content, is of considerable value.

In this study, we investigated the H content in various lunar minerals and the production of H_2O from CE-5 LR at high temperatures through a range of advanced material characterization techniques. The reactions were characterized through several methods, including transmission electron microscopy (TEM), Lorentz TEM, scanning electron microscopy (SEM), energy-dispersive X-ray spectroscopy (EDS), electron energy loss spectroscopy (EELS), X-ray photoelectron spectroscopy (XPS), thermal gravimetric analysis (TGA), vibrating-sample magnetometry, and flash differential scanning calorimetry (DSC). Advanced spherical aberration-corrected TEM, coupled with high EELS, was used to elucidate the evolution of microstructures in lunar particles and the H content. The microstructure, chemical composition, and endogenous reactions of primary lunar minerals, including $FeTiO_3$ ilmenite, olivine, pyroxene, plagioclase, and glass, were examined in detail. This work provides pioneering insights into water production on the Moon through the reaction between H and lunar minerals.

RESULTS AND DISCUSSION

The CE-5 LR is heated above its melting temperature, and its physical properties are studied. Figure 1A shows the XPS of the valence states of iron (Fe) during the heating process. Figure 1B illustrates the concentration of Fe in different valence states—$Fe^{(0)}$, Fe^{2+}, and Fe^{3+}—across a temperature range from room temperature to 1,373 K. Notably, up to 873 K, the $Fe^{(0)}$ content remains largely unchanged, while some Fe^{3+} ions are reduced to Fe^{2+} at around 773 K. At 1,323 K, where the LR melts, ~68.1% of the Fe is reduced to $Fe^{(0)}$, while the contents of Fe^{2+} and Fe^{3+} decrease to 23.2% and 8.7%, respectively. The increase in $Fe^{(0)}$ is attributed to reduction by H, a reaction facilitated by enhanced diffusion in the molten state of the LR.

The amount of $Fe^{(0)}$ is estimated based on magnetic properties. Following the formation of $Fe^{(0)}$, the magnetic moment (M_s) considerably increases from 0.9 to 34.22 emu g^{-1}. For pure Fe, the M_s is ~217 emu g^{-1}.[29] Therefore, the content of $Fe^{(0)}$ in molten LR is ~157 mg g^{-1}. According to the reactions shown in Equations 1 and 2, 1 g of molten LR can generate 51–76 mg of H_2O with 5.62–8.43 mg of H involved in the reaction.

$$FeO + 2H \rightarrow Fe^{(0)} + H_2O \quad \text{(Equation 1)}$$

$$Fe_2O_3 + 6H \rightarrow 2Fe^{(0)} + 3H_2O \quad \text{(Equation 2)}$$

Once the LR melts, the gaseous H_2O can evaporate. At 1,523 K, the weight decreases by ~6.7 wt.% (Figure 1D), which is consistent with the H_2O content estimated from the magnetization data.

After the CE-5 LR is cooled to room temperature, the molten lunar LR transforms into a composite of Fe dendrites embedded in a glassy matrix (Figures 1E–1I). The SEM image in Figure 1E provides a detailed view of the

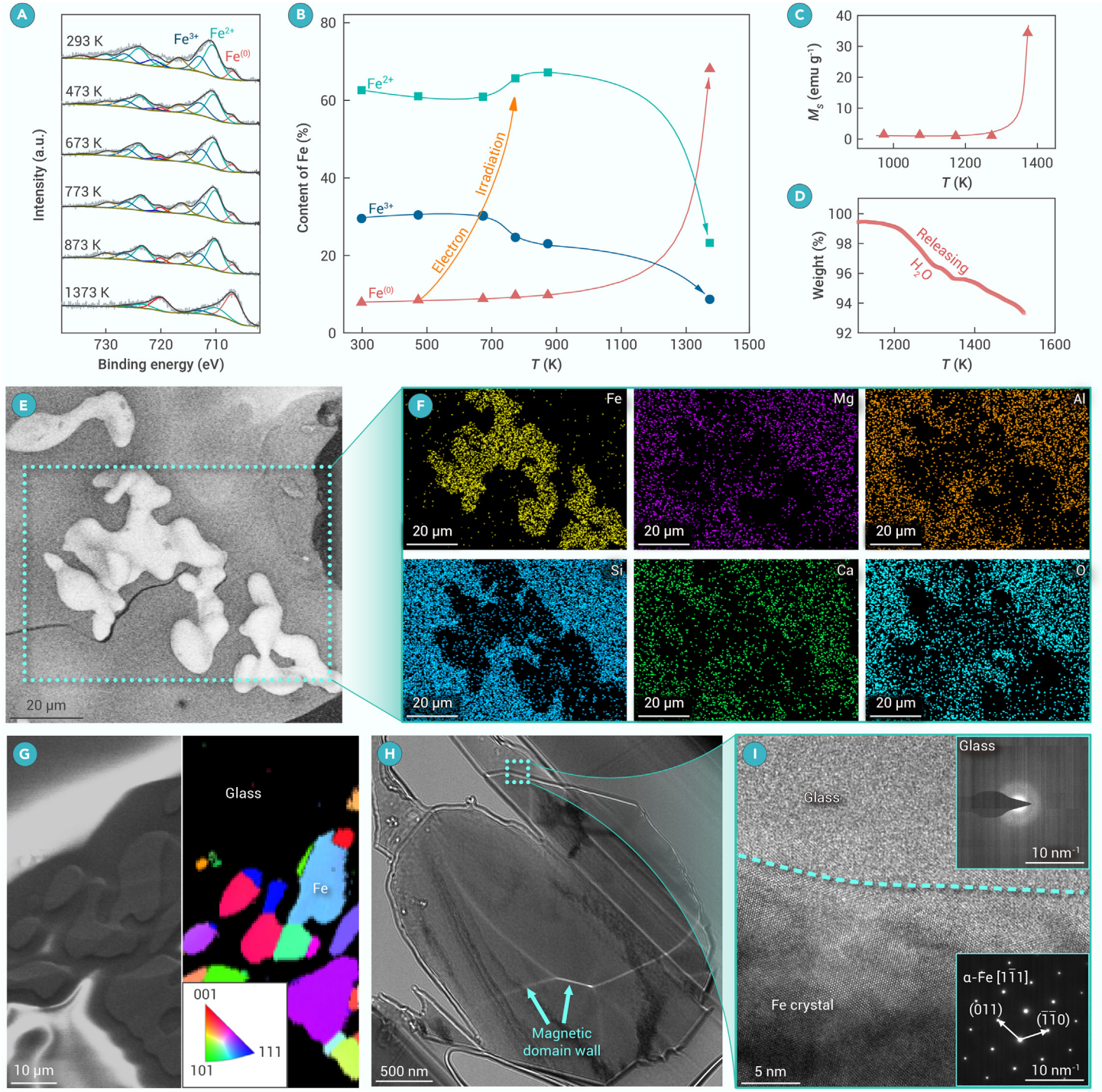

Figure 1. Formation of Fe crystals and water via the heating of lunar regolith (A) XPS spectra of Fe 2p for LR annealed from room temperature to 1,373 K (melting point). (B) Evolution of $Fe^{(0)}$, Fe^{2+}, and Fe^{3+} concentrations derived from (A) as a function of temperature. The orange dashed line indicates that electron irradiation promotes Fe reduction at a lower temperature of ~473 K. (C) Magnetization (M_s) of LR samples annealed at various temperatures (in K). (D) Weight change of LR during heating. (E) SEM image of molten LR showing Fe dendrites embedded in a glassy matrix. (F) EDS mappings of elements for the area highlighted by the purple dashed square in (E). (G) SEM image and corresponding EBSD micrographs of molten LR. In the EBSD image, the colorful regions represent Fe crystals in different orientations, while the dark gray areas denote the glassy matrix. (H) Defocused TEM image of a Fe crystal embedded in the glassy matrix. (I) High-resolution TEM image of the Fe-glass interface.

surface of the LR after the melt has been quenched. Elemental mappings shown in Figure 1F confirm the presence of Fe dendrites, while other elements are distributed homogeneously throughout the matrix. The lattice orientation of the Fe dendrites is examined through electron backscatter diffraction (EBSD; Figure 1G). The EBSD color differentiation highlights the distinct orientations of Fe crystals, with darker areas representing the glassy nature of the matrix. The Lorentz TEM image displays clear magnetic domain walls (Figure 1H), which confirms the ferromagnetism of the Fe dendrites. The high-resolution TEM (HRTEM) image (Figure 1I) reveals the periodic atomic structure of the Fe crystals and the disordered atomic structure of the glassy matrix. These observations are further supported by the selected-area electron diffraction patterns shown in the insets of Figure 1I.

The H content in various lunar minerals is studied. According to previous works,[30,31] the CE-5 LR consists of ~44.5 wt.% pyroxene, 30.4 wt.% plagioclase, 15.5 wt.% glasses, 6.0 wt.% ilmenite, and 3.6 wt.% olivine. As shown in Figure 2A, the peak at 12.5 eV corresponds to the H signal.[32] The integrated area for the EELS peak of H, shown in Figure 2B, represents the concentration of H in various lunar minerals. Among these minerals, $FeTiO_3$ ilmenite has the highest H

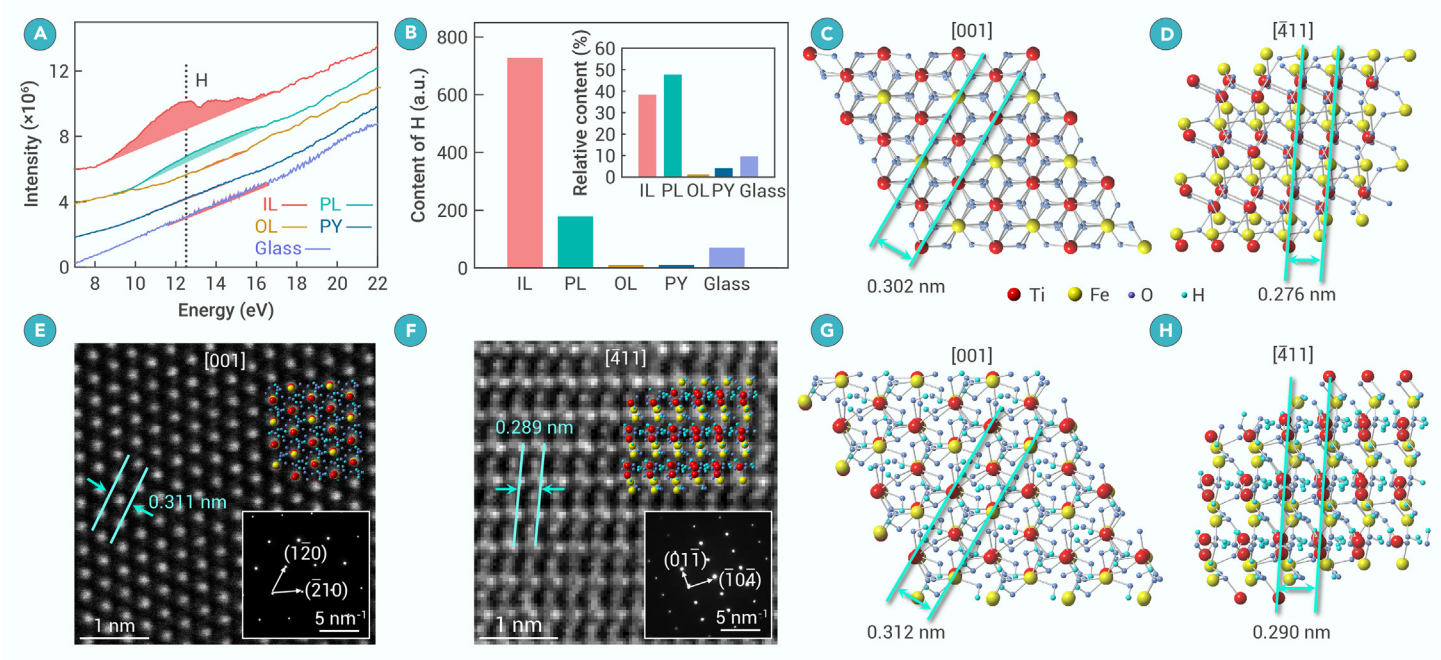

Figure 2. Hydrogen content in lunar minerals (A) EELS peak for hydrogen in different lunar minerals shows that ilmenite (IL) contains the highest hydrogen content. (B) Concentration of hydrogen in different lunar minerals, obtained through the integration of the EELS peak area. The inset shows the weighted hydrogen content in lunar regolith, considering the percentage of each mineral in the overall regolith. (C and D) Ideal atomic packing structure for $FeTiO_3$ IL in projections of [001] and [$\bar{4}$11] orientations. (E and F) High-resolution TEM images for lunar IL in [001] and [$\bar{4}$11] orientations; insets are selected-area electron diffraction patterns. (G and H) Simulated atomic packing structure for lunar $FeTiO_3$ with four injected solar H, which shows similar lattice content to real lunar $FeTiO_3$.

concentration, approximately four times that of plagioclase and over 10 times that of glassy particles. The H concentrations of pyroxene and olivine are negligible compared with those of the other minerals. Considering the abundance of these minerals in LR, a weighted H content is illustrated in the inset of Figure 2B. Despite constituting only 6.0% of the LR, ilmenite retains ~38.3% of the total H content, while plagioclase, which makes up 30.4 wt.% of the regolith, accounts for 47.6% of the total H content.

The atomic packing structure of $FeTiO_3$ ilmenite is examined through HRTEM. The standard lattice structures for $FeTiO_3$ in the [001] and [$\bar{4}$11] orientations are shown in Figures 2C and 2D, respectively. The HRTEM images for these orientations are presented in Figures 2E and 2F. The lattice spacing for lunar ilmenite is slightly larger than the standard lattice spacing. For example, in the [001] orientation, the lattice spacing increases by 3.0%, from 0.302 to 0.311 nm. In the [$\bar{4}$11] orientation, it increases by 4.7%, from 0.276 to 0.289 nm. This expansion is attributable to the injection of H.[33–35] To verify this hypothesis, the atomic packing structure of $FeTiO_3$ doped with H is calculated using density functional theory (Figures 2G and 2H). When four H atoms are introduced into one $FeTiO_3$ unit cell, the lattice constants for the [001] and [$\bar{4}$11] orientations are ~0.312 and ~0.290 nm, respectively, consistent with the TEM results. Notably, most of the H atoms are adsorbed in the sub-nanometer tunnels in the [$\bar{4}$11] orientation (Figures 2F and 2H). The magnetism and TGA results indicate that the total H content in LR is ~0.56 wt.%. EELS data show that 38.3% of this H is captured by ilmenite. Considering that ilmenite constitutes 6.0 wt.% of the LR, the H content in the LR can be calculated as $\frac{0.56\ \text{wt.\%} \times 38.3\%}{6.0\ \text{wt.\%}} = 3.57$ wt.%. The molar mass of $FeTiO_3$ is ~151.7 g/mol, which suggests that there are about 151.7 × 3.57% = 5.4 H atoms per $FeTiO_3$ molecule. This result is consistent with the simulation findings.

Our subsequent investigations focus on the endogenous reaction between implanted H and ilmenite particles at elevated temperatures. Figure 3 displays TEM images of the nanostructures of an ilmenite particle heated to 1,173 K. Numerous nanocrystals (dark particles in Figures 3A and 3B) are uniformly distributed throughout the sample. Notably, all these nanocrystals are associated with a bubble (bright contrast in Figures 3A and 3B) nearby. STEM images (Figures 3C and 3D) further confirm this concurrent nanocrystal-bubble structure, with bright nanocrystals accompanied by dark bubbles. The zoomed-in nanocrystal-bubble structure is further detailed in Figures 3E–3H. EDS mapping (Figure 3I) confirms that these nanocrystals are composed of iron (Fe). Lorentz TEM images (Figure S8) reveal a vortex magnetic domain structure, which is characteristic of magnetic nanocrystals.[36] Point-scanning EELS spectra (Figures 3J and 3K) taken at the bubbles show a peak around 8.5 eV, which indicates the presence of H_2O,[25,37] while the peak for H at 12.5 eV disappears.

The concurrent formation of Fe nanocrystals and H_2O bubbles in ilmenite provides evidence that H, implanted by the solar wind, is a significant resource for producing H_2O. For example, the reaction $FeO + 2H \xrightarrow{\text{high T}} Fe + H_2O$ illustrates this process. Notably, this reaction is not observed in terrestrial $FeTiO_3$ (Figure S10) because it lacks implanted H. However, after H is implanted into terrestrial $FeTiO_3$, the redox reaction occurs (Figure S11). The concurrent formation of Fe nanocrystals and H_2O bubbles is not observed in other LR minerals when heated up to 973 K (Figures S12–S15). Although H retained in plagioclase accounts for nearly 50% of the total H in lunar minerals, the formation of H_2O bubbles is challenging owing to the low H concentration. Nevertheless, at high temperatures, H_2O may aggregate and form bubbles that are subsequently released.

The effect of electron irradiation on H_2O extraction is studied *in situ* using a Spectra 300 transmission electron microscope with a current density of 1.5–2 nA and an acceleration voltage of 300 kV (Figures 4A–4F). At 473 K, bubbles begin to nucleate and expand (Figures 4C–4E, dashed circles). By 773 K, numerous bubbles and dark Fe nanocrystals occur throughout the sample (Figure 4F). A broader perspective (Figure 4G) shows that bubbles form exclusively within the region irradiated by the electron beam, with the boundary outlined by a white dashed line. This effect is attributable to the enhanced atomic diffusivity under electron irradiation. A peak corresponding to H_2O at 8.5 eV is detected in the EELS spectrum within the irradiated zone as shown in the site 1 spectrum in Figure 4I and the spectra in Figure 4K. Notably, the formation temperature of H_2O with electron irradiation (473 K) is considerably lower than that in the absence of irradiation (~873 K; Figures S16 and S17). Thus, electron irradiation effectively promotes H_2O production (Figure 1B, orange curve).

According to the above analysis, we propose a strategy for on-site H_2O extraction on the Moon (Figure 5). LR can be heated by concentrating sunlight using concave mirrors. Once the regolith melts, the H retained in the regolith will react with Fe oxides, producing large amounts of H_2O and Fe. The H_2O vapor is then collected under a cover and pumped into a water tank. This H_2O can meet the needs of humans, animals, and plants. Additionally, the H_2O can be electrochemically decomposed into O_2 and H_2. The O_2 will support life, while the H_2 can provide energy.

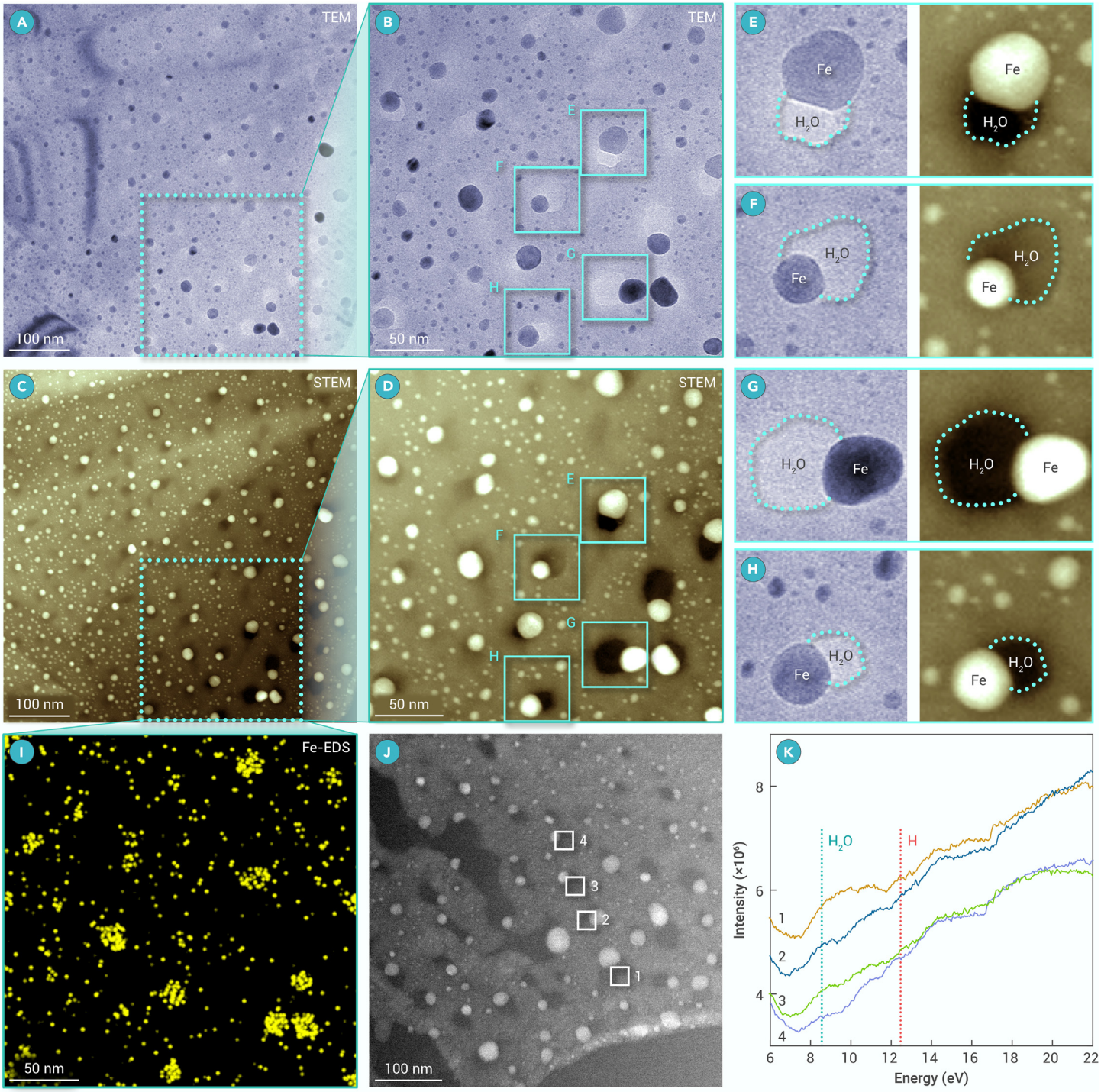

Figure 3. Precipitation of Fe nanocrystal-H_2O bubble pairs in lunar IL (A) TEM image of the IL sample annealed at 973 K. (B) Zoomed-in image of the red dashed square in (A). (C and D) Scanning TEM images corresponding to (A) and (B), respectively. (E–H) Zoomed-in TEM and STEM images of Fe nanocrystal-H_2O bubble pairs in cyan dashed squares within the cyan dashed squares in (B) and (D). Yellow dashed curves outline the borders of the H_2O bubbles. (I) EDS mapping of Fe in the blue dashed square in (C). (J and K) STEM image and EELS spectra at different positions in the annealed IL sample in (J).

A previous study showed that helium atoms mainly formed bubbles and were distributed within the surface amorphous layer of ilmenite particles.[38] In contrast, our observations suggest a more uniform distribution of H ions within ilmenite particles, which extends from the amorphous surface layer to the internal crystalline phases. This solid solution-like dispersion is attributed to the small size and reactive nature of H. Elevated temperatures enable substantial H to react with ilmenite, thus reducing Fe^{2+} to $Fe^{(0)}$ and producing H_2O. This leads to the concurrent formation of Fe nanocrystals and H_2O bubbles. Previous studies[39–42] have suggested transporting H_2 from Earth to the Moon to produce H_2O through reactions with ilmenite. This work, however, demonstrates for the first time that H retained in LR, particularly in $FeTiO_3$ ilmenite, can generate significant amounts of water through endogenous reactions, especially when the regolith is melted at high temperatures or subjected to electron irradiation.

$Fe^{(0)}$ formation cannot be attributed to the disproportionation of Fe^{2+} into $Fe^{(0)}$ and Fe^{3+}, as no detectable presence of $Fe^{(0)}$ or Fe^{3+} is observed in annealed terrestrial ilmenite (Figures S19 and S20). The DSC traces (Figure S19) show neither endothermic nor exothermic reactions. Additionally, the atomic configuration of terrestrial ilmenite remains unchanged after heating to 1,473 K (Figure S20).

Before reaching its molten state, the precipitated Fe nanocrystals are less than 15 nm in diameter and exhibit superparamagnetic behavior. Upon melting, these Fe nanocrystals coalesce to form larger particles or dendrites, which exhibit

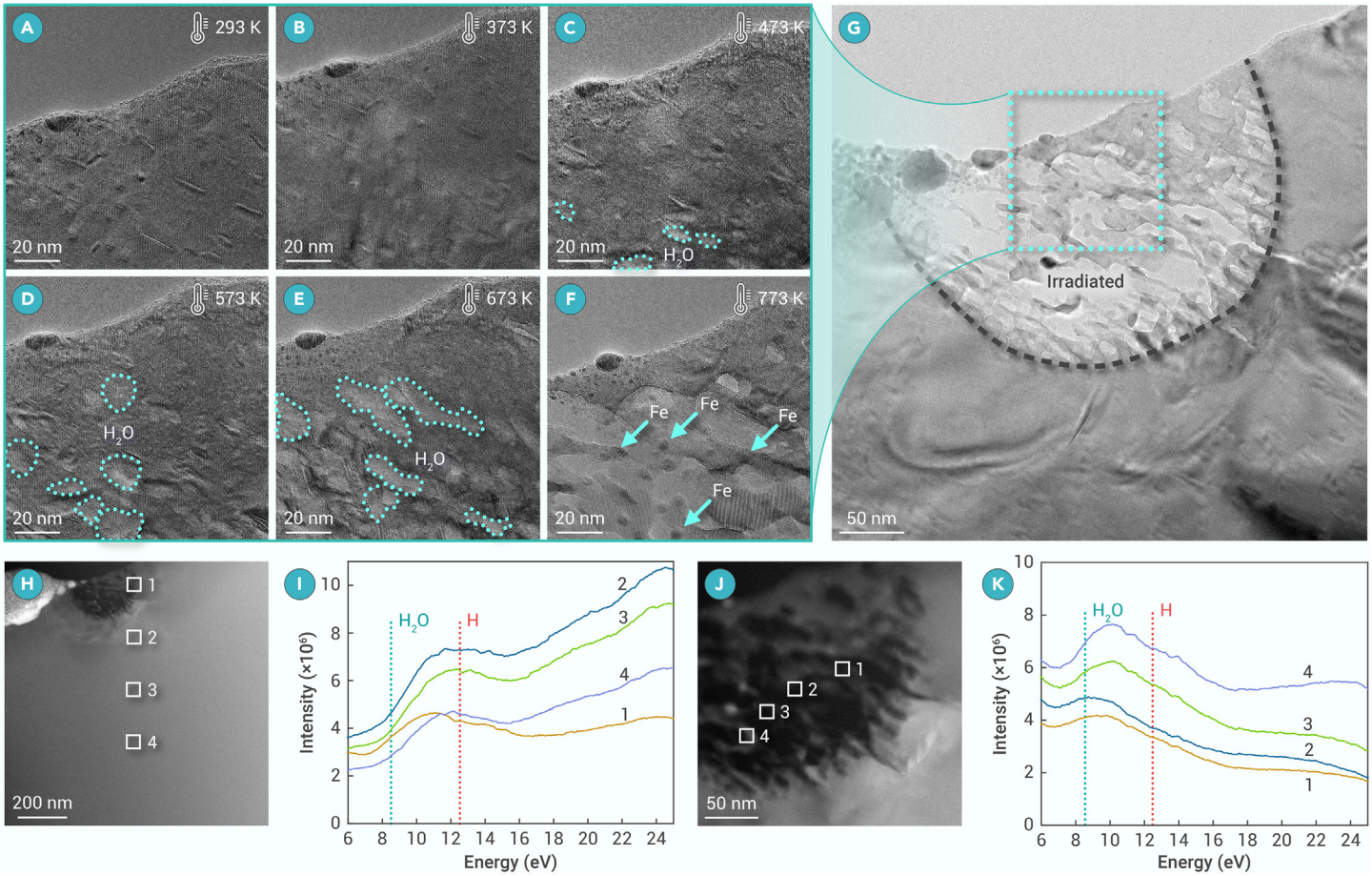

Figure 4. Electron irradiation promoting the reaction of H with IL (A–F) *In situ* HRTEM images of the IL sample at different temperatures ranging from 293 to 773 K, obtained under strong electron irradiation. Yellow dashed circles in (C)–(E) highlight the forming bubbles. Arrows in (F) indicate the Fe nanocrystals. (G) Zoomed-out TEM image after heating, with the electron irradiation-damaged area marked by a white dashed curve. (H and I) EELS spectra from regions close to and outside the irradiated area, with corresponding points indicated on the TEM image. (J and K) EELS spectra within the irradiated area, with corresponding points shown on the TEM image. Peaks at 8.5 and 12.5 eV correspond to H_2O and H_2, respectively.

strong ferromagnetic characteristics, as evidenced by the pronounced magnetization shown in Figure 1C. In contrast, parallel control experiments on terrestrial ilmenite do not reveal any significant change in magnetization (Figure S19). This observation further rules out the possibility of disproportionation reactions of Fe^{2+} in $FeTiO_3$ into $Fe^{(0)}$ and Fe^{3+}.

The abundant formation of encapsulated H_2O bubbles indicates a significant resistance to the release of H_2O gas. This makes it challenging to directly extract H_2O from LR on site. Heating the LR above its melting point of ~1,373 K can facilitate the merging of H_2O bubbles within the molten matrix, thereby aiding in the release of H_2O gas. Previous studies have confirmed that the H-rich LR should be at least 1 m thick.[43–45] The total weight of these regolith deposits is $\sim 5.7 \times 10^{13}$ tons, which can potentially produce around 3×10^{15} kg of water.

Our *in situ* TEM analyses, combined with intense electron irradiation, reveal an accelerated release of entrapped H in LR upon electron exposure. This finding enhances our understanding of the distribution patterns of lunar H_2O and H, indicating that H_2O/OH levels in low-altitude regolith are lower than those in high-altitude regolith.[3,5] This discrepancy is attributable to the more intense solar wind irradiation at lower altitudes, where there are higher concentrations of electrons. Additionally, temperatures at lower altitudes are higher than those at higher altitudes. The combination of high temperatures and strong electron (solar wind) irradiation thus accelerates the release of H_2O/H at lower altitudes on the Moon.

In summary, we observe that a substantial amount of H_2O can be produced via melting CE-5 LR. Our estimates indicate that 1 g of LR could yield ~51–76 mg of H_2O, along with 157 mg of $Fe^{(0)}$. $FeTiO_3$ ilmenite contains the highest H content among the lunar minerals studied. Further investigation of the physical properties of $FeTiO_3$ ilmenite is needed to determine effective methods for separating it from other lunar minerals, which will be valuable for on-site operations on the Moon. Furthermore, our studies highlight the catalytic role of electron irradiation in promoting H release and facilitating H_2O synthesis at lower temperatures. Although LR is relatively dry under ordinary conditions, it could become a significant H_2O reservoir once heated to its melting point. These findings are not only of great interest to geochemistry but also offer valuable insights for future planetary research.

MATERIALS AND METHODS

Sample preparation

The CE-5 lunar samples (CE5C0400) used in this study were collected from the lunar surface and provided by the China National Space Administration. These samples were sealed in a container filled with high-purity argon and then transferred to a glove box with a continuous flow of high-purity argon (Mikrouna) at the Ningbo Institute of Materials Technology & Engineering, Chinese Academy of Sciences. The lunar particles, ranging in size from a few microns to tens of microns, were then placed onto sticky carbon tape. The selected particles were characterized through morphological observation and elemental mapping using a field emission scanning electron microscope (Verios G4 UC, Thermo Scientific) equipped with an EDS detector (X-Man series, Oxford). The measurement parameters were an acceleration voltage of 15.0 kV and a probe current of 3.2 nA. TEM specimens were prepared via the focused ion beam technique (Helios G4 CX, Thermo Scientific). Regions of interest on the selected particles were coated with a thick Pt film (~1 μm) deposited by an ion beam to protect the particle surfaces from damage during ion milling. For specimen heating, the specimens were mounted on a specially designed chip sensor (Thermo Scientific).

Structure and element characterization

The crystal structures of these particles were characterized using a spherical aberration-corrected scanning transmission electron microscope (Spectra 300, equipped with a fifth-order aberration corrector, Thermo Scientific). Measurements were conducted at

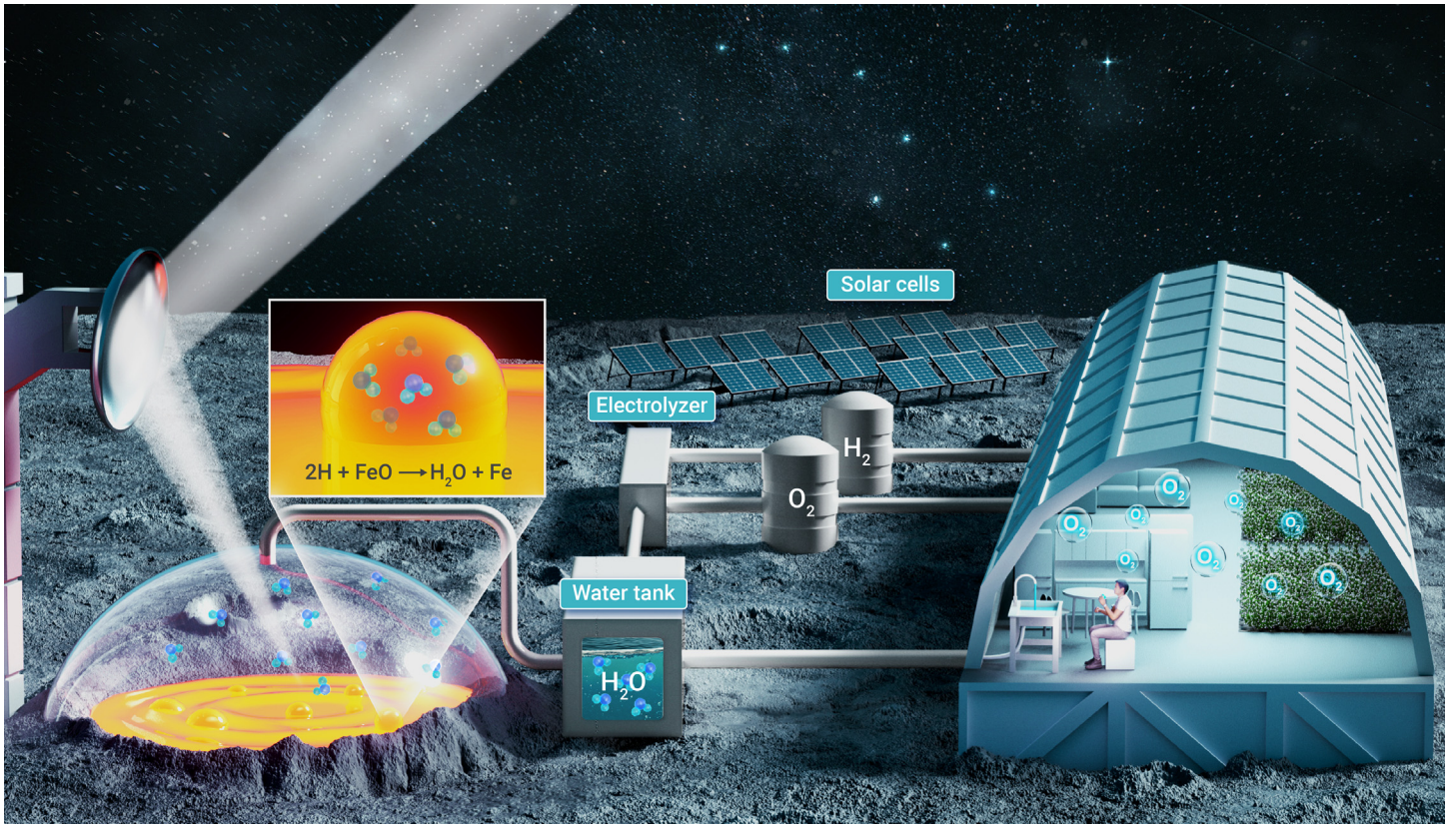

Figure 5. Strategy for on-site H_2O production on the Moon Focused sunlight is used to melt lunar regolith, facilitating the reaction between solar wind-implanted H and Fe oxides to produce water. This water can be used to support life and can also be electrochemically decomposed into oxygen and hydrogen.

an acceleration voltage of 300 kV, and STEM images were acquired in high-angle annular dark field mode. To detect H, EELS was performed using a Gatan 1066 system with a collection semi-angle of 50 rad. The energy resolution, determined by the full width at half maximum of the zero-loss peak, was ~0.3 eV. The elemental content obtained from EDS enabled the classification of lunar particles (Table S1; Figure S1). EDS mapping was conducted using an EDS detector (Thermo Scientific) equipped with four probes. To investigate the effect of electron irradiation, additional TEM was performed using a Talos F200X (Thermo Scientific) operating at an acceleration voltage of 200 kV. Molten LR samples were polished via the broad ion beam technique[46] (TIC 3X series, Leica) at 7 kV for 10 h to prepare them for EBSD. In the EBSD experiments (Symmetry series, Oxford), an accelerating voltage of 20 kV, a working distance of 13 mm, and a step size of 50 nm were used to obtain orientation maps. The valence states of iron in LR were analyzed via XPS (XPS 6I60, Bruker).

Simulation of atomic packing structure of lunar ilmenite

The Vienna *ab initio* simulation package was used to investigate the effects of doping $FeTiO_3$ with H atoms at various ratios, with particular emphasis on the resulting lattice distortions. H atoms were strategically positioned in the largest available interstitial spaces to maintain structural stability. The conjugate gradient algorithm was employed to relax the system. The iterative process for electronic steps was considered complete once the variation in the total energy of the system between successive electronic steps fell below 10^{-6} eV. Conversely, the iteration for ionic steps was terminated after 200 steps. The structural optimization process took into account the antiferromagnetic characteristics of the system. For all computational processes, electron interactions were described using the Perdew-Burke-Ernzerhof functional, a refinement of the generalized gradient approximation for exchange-correlation potential. Owing to the sufficiently large size of the supercell, only the gamma point was considered in the Brillouin zone.

Magnetic property measurement

The magnetic domain structure of the heated LR sample was observed using a Lorentz transmission electron microscope with a customized JEM-2100F.[47] The magnetic properties of LR annealed at different temperatures were measured using a magnetic property measurement system (Quantum Design, measurement precision: $<1 \times 10^{-8}$ emu at H = 0 T; $<8 \times 10^{-8}$ emu at H = 7 T).

Thermal property measurement

Thermal analysis of terrestrial ilmenite was conducted using a differential scanning calorimeter (404F1, Netzsch). The weight loss of LR during the heating process was measured with a simultaneous thermal analyzer (TG-DSC, STA 449F3, Netzsch).

REFERENCES

1. Clark, R.N. (2009). Detection of adsorbed water and hydroxyl on the Moon. Science ***326***(5952): 562–564. https://doi.org/10.1126/science.1178105.
2. Sunshine, J.M., Farnham, T.L., Feaga, L.M., et al. (2009). Temporal and spatial variability of lunar hydration as observed by the Deep Impact spacecraft. Science ***326***(5952): 565–568. https://doi.org/10.1126/science.1179788.
3. Pieters, C.M., Goswami, J.N., Clark, R.N., et al. (2009). Character and spatial distribution of OH/H_2O on the surface of the Moon seen by M3 on Chandrayaan-1. Science ***326***(5952): 568–572. https://doi.org/10.1126/science.1178658.
4. Bandfield, J.L., Poston, M.J., Klima, R.L., et al. (2018). Widespread distribution of OH/H_2O on the lunar surface inferred from spectral data. Nat. Geosci. ***11***: 173–177. https://doi.org/10.1038/s41561-018-0065-0.
5. Li, S., and Milliken, R.E. (2017). Water on the surface of the Moon as seen by the Moon Mineralogy Mapper: distribution, abundance, and origins. Sci. Adv. ***3***(9): e1701471. https://doi.org/10.1126/sciadv.1701471.
6. Wohler, C., Grumpe, A., Berezhnoy, A.A., et al. (2017). Time-of-day-dependent global distribution of lunar surficial water/hydroxyl. Sci. Adv. ***3***(9): e1701286. https://doi.org/10.1126/sciadv.1701286.
7. Liu, Y., Guan, Y., Zhang, Y., et al. (2012). Direct measurement of hydroxyl in the lunar regolith and the origin of lunar surface water. Nat. Geosci. ***5***(11): 779–782. https://doi.org/10.1038/ngeo1601.
8. Saal, A.E., Hauri, E.H., Van Orman, J.A., et al. (2013). Hydrogen isotopes in lunar volcanic glasses and melt inclusions reveal a carbonaceous chondrite heritage. Science ***340***(6138): 1317–1320. https://doi.org/10.1126/science.1235142.
9. Hui, H., Peslier, A.H., Zhang, Y., et al. (2013). Water in lunar anorthosites and evidence for a wet early Moon. Nat. Geosci. ***6***(3): 177–180. https://doi.org/10.1038/ngeo1735.
10. Yang, W., and Lin, Y. (2021). New lunar samples returned by Chang'e-5: opportunities for new discoveries and international collaboration. Innovation ***2***(1): 100070. https://doi.org/10.1016/j.xinn.2020.100070.
11. Izawa, M.R., Cloutis, E.A., Applin, D.M., et al. (2014). Laboratory spectroscopic detection of hydration in pristine lunar regolith. Earth Planet Sci. Lett. ***390***: 157–164. https://doi.org/10.1016/j.epsl.2014.01.007.

12. Lin, H., Li, S., Xu, R., et al. (2022). In situ detection of water on the Moon by the Chang'E-5 lander. Sci. Adv. ***8***(1): eabl9174. https://doi.org/10.1126/sciadv.abl9174.
13. Zhou, C., Tang, H., Li, X., et al. (2022). Chang'E-5 samples reveal high water content in lunar minerals. Nat. Commun. ***13***(1): 5336. https://doi.org/10.1038/s41467-022-33095-1.
14. Xu, Y., Tian, H.C., Zhang, C., et al. (2022). High abundance of solar wind-derived water in lunar soils from the middle latitude. Proc. Natl. Acad. Sci. USA ***119***(51): e2214395119. https://doi.org/10.1073/pnas.2214395119.
15. He, H., Ji, J., Zhang, Y., et al. (2023). A solar wind-derived water reservoir on the Moon hosted by impact glass beads. Nat. Geosci. ***16***(4): 294–300. https://doi.org/10.1038/s41561-023-01159-6.
16. Hu, S., He, H., Ji, J., et al. (2021). A dry lunar mantle reservoir for young mare basalts of Chang'e-5. Nature ***600***(7887): 49–53. https://doi.org/10.1038/s41586-021-04107-9.
17. Li, Q.L., Zhou, Q., Liu, Y., et al. (2021). Two-billion-year-old volcanism on the Moon from Chang'e-5 basalts. Nature ***600***(7887): 54–58. https://doi.org/10.1038/s41586-021-04100-2.
18. Schaible, M.J., and Baragiola, R.A. (2014). Hydrogen implantation in silicates: the role of solar wind in SiOH bond formation on the surfaces of airless bodies in space. JGR. Planets ***119***(9): 2017–2028. https://doi.org/10.1002/2014je004650.
19. Tang, H., Li, X., Zeng, X., et al. (2021). Experimental investigation of structural OH/H_2O in different lunar minerals and glass via solar-wind proton implantation. Icarus ***359***: 114322. https://doi.org/10.1016/j.icarus.2021.114322.
20. Stephant, A., and Robert, F. (2014). The negligible chondritic contribution in the lunar soils water. Proc. Natl. Acad. Sci. USA ***111***(42): 15007–15012. https://doi.org/10.1073/pnas.1408118111.
21. Epstein, S., and Tayor, H.P., Jr. (1970). The concentration and isotopic composition of hydrogen, carbon and silicon in Apollo 11 lunar rocks and minerals in Proc. Apollo II Lunar. Sci. Conf. Geochim. Cosmochim. Acta. ***1***: 1085–1086.
22. Epstein, S., and Tayler, H.P., Jr. (1973). The isotopic composition and concentration of water, hydrogen, and carbon in some Apollo 15 and 16 soils and in the Apollo 17 orange soil in Proc. 4th Lunar Sci. Conf. ***4***: 1559–1575.
23. Friedman, I., O'neil, J.R., Adami, L.H., et al. (1970). Water, hydrogen, deuterium, carbon, carbon-13, and oxygen-18 content of selected lunar material. Science ***167***(3918): 538–540. https://doi.org/10.1126/science.167.3918.538.
24. Managadze, G.G., Cherepin, V.T., Shkuratov, Y.G., et al. (2011). Simulating OH/H_2O formation by solar wind at the lunar surface. Icarus ***215***(1): 449–451. https://doi.org/10.1016/j.icarus.2011.06.025.
25. Bradley, J.P., Ishii, H.A., Gillis-Davis, J.J., et al. (2014). Detection of solar wind-produced water in irradiated rims on silicate minerals. Proc. Natl. Acad. Sci. USA ***111***(5): 1732–1735. https://doi.org/10.1073/pnas.1320115111.
26. Zeng, X., Tang, H., Li, X., et al. (2021). Experimental investigation of OH/H_2O in H^+-irradiated plagioclase: implications for the thermal stability of water on the lunar surface. Earth Planet Sci. Lett. ***560***: 116806. https://doi.org/10.1016/j.epsl.2021.116806.
27. Qian, Y., Xiao, L., Wang, Q., et al. (2021). China's Chang'e-5 landing site: geology, stratigraphy, and provenance of materials. Earth Planet Sci. Lett. ***561***: 116855. https://doi.org/10.1016/j.epsl.2021.116855.
28. Tian, H.C., Wang, H., Chen, Y., et al. (2021). Non-KREEP origin for Chang'e-5 basalts in the Procellarum KREEP Terrane. Nature ***600***(7887): 59–63. https://doi.org/10.1038/s41586-021-04119-5.
29. Coey, J.M.D. (2010). Magnetism and Magnetic Materials (Cambridge University Press), pp. 384–398. https://doi.org/10.1017/CBO9780511845000.
30. Zhang, H., Zhang, X., Zhang, G., et al. (2021). Size, morphology, and composition of lunar samples returned by Chang'E-5 mission. Sci. China Phys. Mech. Astron. ***65***(2): 8. https://doi.org/10.1007/s11433-021-1818-1.
31. Li, C., Hu, H., Yang, M.F., et al. (2022). Characteristics of the lunar samples returned by the Chang'E-5 mission. Natl. Sci. Rev. ***9***(2): nwab188. https://doi.org/10.1093/nsr/nwab188.
32. Ahn, C., and Krivanek, O.L. (1983). EELS Atlas: A Reference Guide of Electron Enery Loss Spectra Covering All Stable Elements (Joint Project of the ASU HREM Facility and GATAN).
33. Liu, G., Zhou, W., Ji, Y., et al. (2021). Hydrogen-intercalation-induced lattice expansion of Pd@Pt core-shell nanoparticles for highly efficient electrocatalytic alcohol oxidation. J. Am. Chem. Soc. ***143***(29): 11262–11270. https://doi.org/10.1021/jacs.1c05856.
34. Xie, M., Zhang, B., Jin, Z., et al. (2022). Atomically reconstructed palladium metallene by intercalation-induced lattice expansion and amorphization for highly efficient electrocatalysis. ACS Nano ***16***(9): 13715–13727. https://doi.org/10.1021/acsnano.2c05190.
35. Wang, Y., Jiao, Y., Yan, H., et al. (2022). Vanadium-incorporated CoP_2 with lattice expansion for highly efficient acidic overall water splitting. Angew. Chem., Int. Ed. Engl. ***61***(12): e202116233. https://doi.org/10.1002/anie.202116233.
36. Kittel, C. (1949). Physical theory of ferromagnetic domains. Rev. Mod. Phys. ***21***(4): 541–583. https://doi.org/10.1103/RevModPhys.21.541.
37. Grand, D., Amouyal, E., and Bernas, A. (1979). Photoionization of aqueous indole: conduction band edge and energy gap in liquid water. Chem. Phys. ***44***(1): 73–79. https://doi.org/10.1016/0301-0104(79)80064-6.
38. Li, A., Chen, X., Song, L., et al. (2022). Taking advantage of glass: capturing and retaining the helium gas on the moon. Mater. Futur. ***1***(3): 035101. https://doi.org/10.1088/2752-5724/ac74af.
39. Li, Y., Li, X., Wang, S., et al. (2012). In-situ water production by reducing ilmenite. In Moon: Prospective Energy and Material Resources, V. Badescu, ed. (Springer Berlin Heidelberg), pp. 189–200. https://doi.org/10.1007/978-3-642-27969-0_8.
40. Crawford, I.A. (2015). Lunar resources: a review. Prog. Phys. Geogr. ***39***(2): 137–167. https://doi.org/10.1177/0309133314567585.
41. Xiao, W., Lu, X.-G., Zou, X.-L., et al. (2014). Multiple gaseous reduction of ilmenite: thermodynamic and experimental study. Rare Met. ***34***(12): 888–894. https://doi.org/10.1007/s12598-014-0264-9.
42. Sargeant, H.M., Abernethy, F.A.J., Barber, S.J., et al. (2020). Hydrogen reduction of ilmenite: Towards an in situ resource utilization demonstration on the surface of the Moon. Planet. Space Sci. ***180***: 104751. https://doi.org/10.1016/j.pss.2019.104751.
43. Feldman, W.C., Maurice, S., Lawrence, D.J., et al. (2001). Evidence for water ice near the lunar poles. J. Geophys. Res. ***106***(E10): 23231–23251. https://doi.org/10.1029/2000je001444.
44. Mitrofanov, I.G., Sanin, A.B., Boynton, W.V., et al. (2010). Hydrogen mapping of the lunar south pole using the LRO neutron detector experiment LEND. Science ***330***(6003): 483–486. https://doi.org/10.1126/science.1185696.
45. Tian, H.C., Hao, J., Lin, Y., et al. (2024). Distribution and abundance of solar wind-derived water in Chang'E-5 core samples and its implications. Geophys. Res. Lett. ***51***(9): e2023GL107005. https://doi.org/10.1029/2023gl107005.
46. Jiang, R., Li, M., Yao, Y., et al. (2019). Application of BIB polishing technology in cross-section preparation of porous, layered and powder materials: a review. Front. Mater. Sci. ***13***(2): 107–125. https://doi.org/10.1007/s11706-019-0457-0.
47. Pei, K., Xia, W.-X., Wang, B.-M., et al. (2018). Investigation of magnetization reversal process in pinned CoFeB thin film by in-situ Lorentz TEM. Chin. Phys. B ***27***(4): 047502. https://doi.org/10.1088/1674-1056/27/4/047502.

ACKNOWLEDGMENTS

We thank all the staff of the Chang'E Lunar Exploration Project for their work in returning lunar samples and the China National Space Administration (CNSA) for providing the lunar sample. Discussions with Prof. Fang Fang about hydrogen storage in materials is acknowledged. Financial support from the National Key R&D Program of China (2018YFA0703600), the National Natural Science Foundation of China (NSFC 52222105, 51922102, 92163108, 61888102, and 51827801), the Youth Innovation Promotion Association CAS (2019296), the Zhejiang Provincial Natural Science Foundation of China (LZ22A030001 and LR22E010004), and the Ningbo 2025 Science and Technology Innovation Project is acknowledged.

AUTHOR CONTRIBUTIONS

W.H.W., H.Y.B., M.F.Y., and Z.G.Z. led this project. J.Q.W. and J.T.H. conceived and guided the research. X.C., W.X., J.Q.W., and J.T.H. designed the experiments. X.C., L.J.S., M.G., and L.Z. prepared the samples. X.C., G.X.C., W.X.X., M.L., H.C.W., J.F.C., and P.L.K. conducted the TEM and EELS measurements. S.Y.Y. did the simulation work. X.C. and L.J.M. did the XPS analysis. X.C., J.-Q.W., X.X.S., W.P.X. and P.L.K. did the thermal analysis. Y.J.H. and J.F.S. did the proton irradiation experiments. All authors discussed the results and contributed to the preparation of the manuscript. J.Q.W., X.C., J.T.H., H.Y.B. and W.H.W. wrote the manuscript.

DECLARATION OF INTERESTS

The authors declare no competing interests.

SUPPLEMENTAL INFORMATION

It can be found online at https://doi.org/10.1016/j.xinn.2024.100690.

LEAD CONTACT WEBSITE

https://non-crystal.nimte.ac.cn/